Hard-yet-tough high-vanadium hierarchical composite coating

Cao, H. T.; Dong, X. P.; Chabok, A.; Rao, J. C.; De Hosson, J. Th M.; Pei, Y. T.

Published in:
Materials science and engineering a-Structural materials properties microstructure and processing

DOI:
10.1016/j.msea.2018.08.086

Publication date:
2018

Materials Science & Engineering A 736 (2018) 87–99

Contents lists available at ScienceDirect

Materials Science & Engineering A

journal homepage: www.elsevier.com/locate/msea

Hard-yet-tough high-vanadium hierarchical composite coating: Microstructure and mechanical properties

H.T. Cao[a,b,*], X.P. Dong[b], A. Chabok[a], J.C. Rao[c,d], J. Th.M. De Hosson[d], Y.T. Pei[a,**]

[a] Department of Advanced Production Engineering, Engineering and Technology Institute Groningen, University of Groningen, Nijenborgh 4, 9747 AG, the Netherlands
[b] State Key Laboratory of Materials Processing and Die & Mould Technology, School of Materials Science and Engineering, Huazhong University of Science and Technology, Wuhan 430074, China
[c] AIM Lab, Maryland NanoCenter, University of Maryland, College Park, MD 20742, USA
[d] Department of Applied Physics, Zernike Institute for Advanced Materials, University of Groningen, Nijenborgh 4, 9747 AG Groningen, the Netherlands

ARTICLE INFO

Keywords:
Plasma surface alloying
Vanadium
MC carbides
Hard-yet-tough
Fracture
Crack resistance

ABSTRACT

In this work, we report a high-vanadium hierarchical coating prepared on the surface of nodular cast iron substrate by a low-cost plasma transferred arc (PTA) surface alloying process. The coating consists of a graded layer with an alloyed zone (AZ) rich in submicron sized granular (V-Ti-Nb-Cr-Mo) composite carbides on top of intermediate melted zone characterized by refined ledeburite and martensite. The dense spherical particles in the AZ are FCC structured MC-type (M = V, Ti and Nb) carbides which tend to aggregate while M_7C_3 and M_2C carbides nucleate on MC. The super-lattice V_8C_7 maintains its cube-on-cube orientation relationship with TiC. The hardness of the AZ is 9.6 ± 1.0 GPa, ~ 4 times that of the substrate. Nano- and micro-indentations point at a superior strength-toughness in the AZ, where cracks are deflected and bridged by the spherical MC carbides in a compressive residue stress state. The fracture mode appears to be rather ductile in the AZ whereas brittle failure appears in both the melted zone and substrate. TEM and EDS results confirm that such a micro-architecture design, assisted by the rapid solidification rate of the PTA process, concurrently activates various strengthening micromechanisms including the precipitation hardening and grain refinement.

1. Introduction

The growing ecological and economic concerns inspire materials engineers to develop novel corrosion-, fatigue- and wear-resistant protective coatings to strengthen the surface of weaker bulk materials. Generally speaking, coatings to be used in diverse environmental testing conditions need to be hard and sufficiently tough to withstand impact loading and resist abrasion and propagation of cracks. In the field of surface engineering, research has been toward modifying the surface with hard ceramic nitrides or carbides such as Si_3N_4, WC, Cr_7C_3 to strengthen the weak surface. However, the "strength-ductility trade-off" remains a bottleneck to achieve in such single-phase monolithic binary ceramics [1,2]. For instance, a single Cr-reinforced alloy design strengthens the base material but readily leads to the build-up of damage during services in practice because of the substantial brittleness induced by its elongated and/or block-shaped M_7C_3 carbides [3,4].

To beat the conventional rule that improving the strength of metallic alloys involves a tradeoff in a loss of ductility, there has been intensive interests in exploring multi-constituent structure to induce exceptional strength-ductility-toughness combination [1,5]. For instance, high-entropy alloy (HEA) consists of five or more principal elements at equimolar or near-equimolar compositions yielding single-phase (e.g. FCC or BCC) solid solutions that they benefit from phase stabilization via entropy maximization and in turn contribute to the strength-ductility property [6–8].

Alternatively, in steels hybrid metastable alloys can be tuned so as to have a wide range of unexpected properties [5,9,10]. The hard-yet-tough approach can even be bio-inspired by the toughening strategy effective in many natural hierarchical composites that incorporate strong-yet-brittle minerals into soft organic matrices [11–15]. Strong building blocks offer high strength and stiffness while the soft components maintain the integrity and impart toughness and ductility [13,16,17]. Other example comprises the refractory ceramic carbides of group IV–V transition metals, such as VC, TiC and NbC, i.e. a family of

* Corresponding author at: Department of Advanced Production Engineering, Engineering and Technology Institute Groningen, University of Groningen, Nijenborgh 4, 9747 AG, the Netherlands.
** Corresponding author.
E-mail addresses: huatang.cao@rug.nl (H.T. Cao), y.pei@rug.nl (Y.T. Pei).

https://doi.org/10.1016/j.msea.2018.08.086
Received 4 July 2018; Received in revised form 23 August 2018; Accepted 24 August 2018
Available online 28 August 2018
0921-5093/

materials sharing a NaCl-type crystal structure. They all demonstrate a high melting point (2810–3490 °C), high microhardness (2400–3200 HV), excellent chemical durability, high wear and corrosion resistance [10,18–21]. Additional Cr and Mo elements into alloys induce massive solution strengthening and secondary hardening, which further enhance the hardness and the high-temperature oxidation resistance [22,23].

A promising candidate to offer the aforementioned various carbides is the high-speed steel (HSS) [24–26]. In particular, the high-vanadium high-speed steels (HVHSS) having a vanadium content up to 9–15 wt%, stands out because of its large amount of strong VC carbides dispersed in a matrix of ferrite or austenite [22,27,28]. The VC-type carbide is particularly intriguing due to its manifold practical advances of favorably spherical shape and good wettability to ferrous materials on top of exceptional hardness and high melting point [29–32].

Therefore, this study explores a hybrid (V-Ti-Nb-Cr-Mo)-containing metallurgical HVHSS coating made by an atmospheric plasma transferred arc (PTA) alloying (instead of conventional casting technique) on a nodular cast iron (NCI). The latter is a rather inexpensive and widely used engineering material with a good strength-toughness due to ferrite and graphitic nodules. We have developed a HVHSS–modified white iron–NCI graded microarchitecture. The key point of such HVHSS strategy is to introduce directly from the melt a sufficiently high density of ultrafine hard carbides with ideal shape and distribution in a soft and ductile matrix, thereby yielding an enhanced strength without compromising the toughness.

2. Experimental procedure

2.1. Material preparations

Nodular cast iron with a composition of Fe-3.7C-2.7Si-0.3Mn (wt%) was employed as substrate for plasma surface alloying (PSA). The dimensions of the nodular cast iron substrate were 100 mm × 50 mm × 20 mm. The microstructure of the substrate consists of graphite nodules embedded in pearlitic regions and a ferritic matrix, as shown in Fig. 1a. The diameter of the graphite nodules ranges from 20 to 50 μm. The inset of Fig. 1a presents a close-up of the lamellar pearlite. The alloying powders (all purities ≥ 99.0%) consist of ferrovanadium (FeV50), ferroniobium (FeNb60) and pure titanium, chromium, molybdenum and were mixed in a weight ratio of 10V-4Cr-3Ti-3Mo-2Nb. The carbon source for forming carbides stems from the NCI substrate (namely the graphite nodules). This procedure allows an in-situ synthesis of hard phases favoring reinforcements with strong interface bonding. Powders were mechanically blended in a planetary ball mill to reduce their size to < 5 μm, as shown in Fig. 1b. The powders were then sprayed onto the polished NCI substrate to form a coating layer with a thickness of 25–50 μm, followed by drying treatment in a furnace for 30 min at 150 °C. Thereafter a homemade plasma beam apparatus was employed as a heating source to produce the coatings due to its advantages of high energy efficiency, the feasibility of working in an air atmosphere and competitive running costs [1,33,34]. For more details about the plasma apparatus reference is made to [35]. Details of the processing parameters are listed in Table 1. Argon was used as a shielding gas to prevent oxidation during the PSA treatment.

2.2. Materials characterization

After the PSA treatment, transverse cross-sections of coated samples were prepared by standard mechanical grinding, polishing and etching with 4 wt% nital. The microstructure was examined with scanning electron microscopy (SEM, FEI XL30-FEG and Tescan Lyra) equipped with energy dispersive spectrometer (EDS, EDAX) and transmission electron microscopy (TEM, JEOL 2010-FEG) enabled with a Bruker EDS detector. Phase structures were identified by an X-ray diffractometer (XRD, Bruker D8 Advance) using Cu Kα radiation. The sample was scanned over a 2θ range from 20° to 90° with a step size of 0.025° and a large time lapse of 15 s (total testing time: 12 h) for a better interpretation of the formed miscellaneous phases. The nano-hardness of the plasma alloyed, melted zones and NCI substrate was measured with a MTS Nanoindenter XP® equipped with a Berkovich indenter (displacement-control mode, maximum indentation depth 800 nm). An atomic force microscope (AFM, Dimension 3100) was used to plot the morphology of the indents after the nanoindentation. Furthermore, a Vickers hardness tester was used to induce heavy deformations to estimate crack resistance under a high load of 50 N. Room-temperature fracture morphologies (induced by the mechanical bending) were also examined to investigate the failure modes of the three regions of the coating. Micro-slit milling (Ga^+, 30 kV) with a focused ion beam (dual-beam FIB-SEM, Tescan) system was employed to measure the local magnitude of residual stress in both the alloying zone and the melted zone. First, the surface of the specimen was densely decorated with yttrium-stabilized zirconia (YSZ) nano-particles to offer sufficiently random and high-contrast features suitable for effective digital image correlation (DIC). An area of interest is imaged by the SEM, and thereafter the sample is tilted by 55°, such that the same surface area is

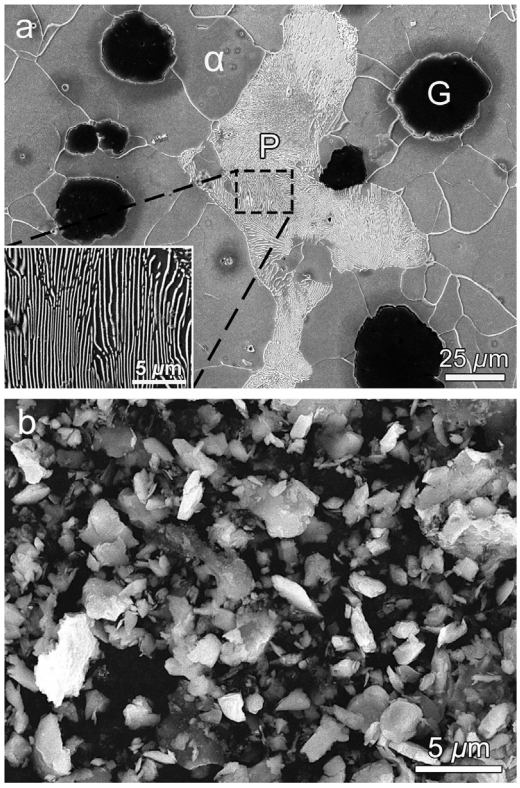

Fig. 1. SEM images of (a) as-received nodular cast iron with the inset showing the enlarged lamellar pearlite (P: pearlite; G: graphite; α: ferrite) and (b) the raw mixed powders with size below 5 μm after ball milling.

Table 1
PTA experimental parameters.

Parameters	Value
Transferred arc current (A)	100
Plasma gas flux (Ar) ($L\,min^{-1}$)	6
Shielding gas flux (Ar) ($L\,min^{-1}$)	3
Scanning speed ($mm\,min^{-1}$)	900–1600
Diameter of the torch (mm)	4
Working distance (mm)	4
Overlapping rate	25%

oriented normal to the FIB and milled by Ga^+ ion beam. Slits were milled with a width of 0.5 μm, depth of 3 μm and length of 30 μm. After that, the sample was titled back to 0° to capture the identical region after milling. The displacement field perpendicular to the plane of slit was detected via DIC by comparisons of SEM images (768 × 768 pixels) before and after milling. DIC was performed using software GOM Correlate 2016. The magnitude of residual stress perpendicular to the plane of the slit was determined by empirically fitting the experimentally detected displacements with the displacements calculated from the analytical solution for an infinite length slit in an isotropic linear elastic material [36]:

$$U_{dir}(\mathrm{d}) = \frac{2.243}{E'}\sigma_{dir}\int_0^{a_f} cos\theta\left(1+\frac{sin^2\theta}{2(1-\nu)}\right)\times(1.12 + 0.18\cdot\mathrm{sech}(\tan\theta))da \quad (1)$$

where a_f is the depth of the slit; $E' = E/(1-\nu^2)$, with E being the Young's modulus and ν the Poisson's ratio; $\theta = \arctan(\mathrm{d}/a)$, with d the distance to the slit and a changing between 0 and a_f, and *dir* represents x or y direction.

3. Results

3.1. Microstructure evolution

The cross-sectional SEM micrograph in Fig. 2a shows the microstructural evolutions along the depth of the graded coating about 0.35 mm thick. It can be divided into three regions: (1) the top alloyed zone (AZ), (2) the intermediate melted zone (MZ) and (3) the heat-affected zone (HAZ). The plasma energy is applied to melt simultaneously the preplaced powder and the substrate, leading to this graded structure of three distinct zones. Fig. 2b indicates the linear elemental distribution (V, Cr, Mo, Ti, Nb, Fe and C) versus the depth of the cross-section. The content of V is the highest in the AZ, followed by Cr. The content of Ti together with Mo and Nb hardly changes in the AZ before dropping to zero in MZ. The gradual chemical composition transition from the AZ to the MZ confirms a good metallurgical bonding. Besides, Cr-rich phases form at the interface (see Fig. 2b), which were reported to promote the coating adhesion onto ferrous substrates [37]. Fig. 2c–e are SEM close-ups of the AZ, the MZ and the HAZ. The AZ contains a large proportion of dark particles that are homogeneously dispersed in the matrix, spheroidal and of submicrometer size, as seen in Fig. 2c. Dendrites or cellular microstructure are not observed, which were reported in many other metallurgical hardfacings clad by laser or plasma arc [24,38,39]. Fig. 2d and e indicate that the MZ consists of a fine typical white iron structure (ledeburite) reinforced with martensite, whereas the HAZ is characteristic of twined martensite (Z-shaped or lenticular) and ledeburite double shells together with graphite nodules of dwindled size. The microstructures in the MZ and the HAZ are discussed in details in our previous publications [35,40,41]. The less visible grain boundaries in the AZ as compared with that in the MZ and HAZ indicate enhanced corrosion resistance of the coating induced by the hybrid alloy elements (particularly Cr).

Backscattered electrons SEM micrograph in Fig. 3a shows that various submicron-sized spheroidal particles colored at different gray scales are dispersed in the coating. Meanwhile, some whitish blocky or strip-shaped carbides connecting or surrounding the dark ones are observed. Fig. 3b and c–h show the overlaid and individual EDS mapping of elements. Fig. 3a–f display the spherical dispersed particles are predominantly V-rich phases (colored in blue), partly doped with Ti (colored in red) and Nb (colored in yellow) and the carbon element resembles similar distribution. Therefore the dark particles in the AZ are determined as MC-type carbides, particularly VC considering the high content of V as verified in Fig. 3d. Fig. 3g and h confirm that Cr and Mo elements tend to agglomerate in the platelike carbides (e.g. M_7C_3 and M_2C) around the MC carbides [40]. Note that similar bulk-shaped Fe-rich cementite also exists as indicated in Fig. 3a. In comparison with Fig. 3a, g and h manifest that apart from forming carbides, Cr with partial Mo scatters over the entire AZ area, indicating the solid solution of some Cr and Mo into the matrix. Fig. 3i confirms the highest content of V (13.5 at%) and the second highest of Cr (9.3 at%), and Ti, Mo and Nb below 3 at% in the whole area of Fig. 3a, respectively. Careful observations on Fig. 3d–f reveal that the Nb element has a similar distribution with V although its intensity is much lower. This suggests a potential miscibility of VC-NbC crystals [39]. The content of Ti is, however, rather high in the center of some of the spherical MC particles. Both V and Ti are not observed in the matrix as compared with Cr and Mo.

Previous studies [11,39] pointed out that the predominant effect of vanadium in HSSs is to form MC-type carbides. Here, we propose that

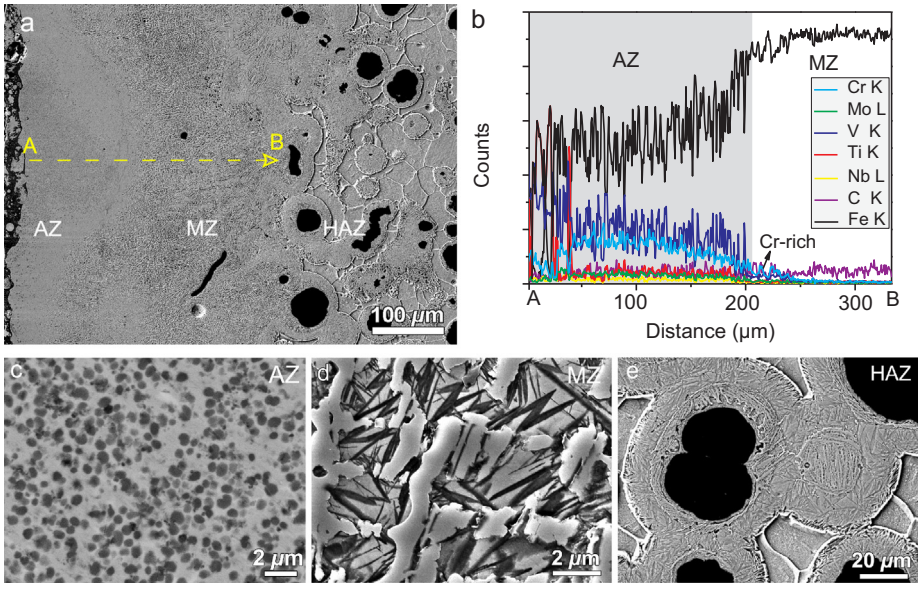

Fig. 2. (a) SEM micrograph showing the cross-section of the coating and (b) linear EDS scan along the line A–B marked in (a); Close view of the microstructure of the AZ (c), MZ (d) and HAZ (e), respectively. Compared with MZ and HAZ, the AZ appears potentially more corrosion-resistant due to less visible grain boundaries revealed after being etched with nital.

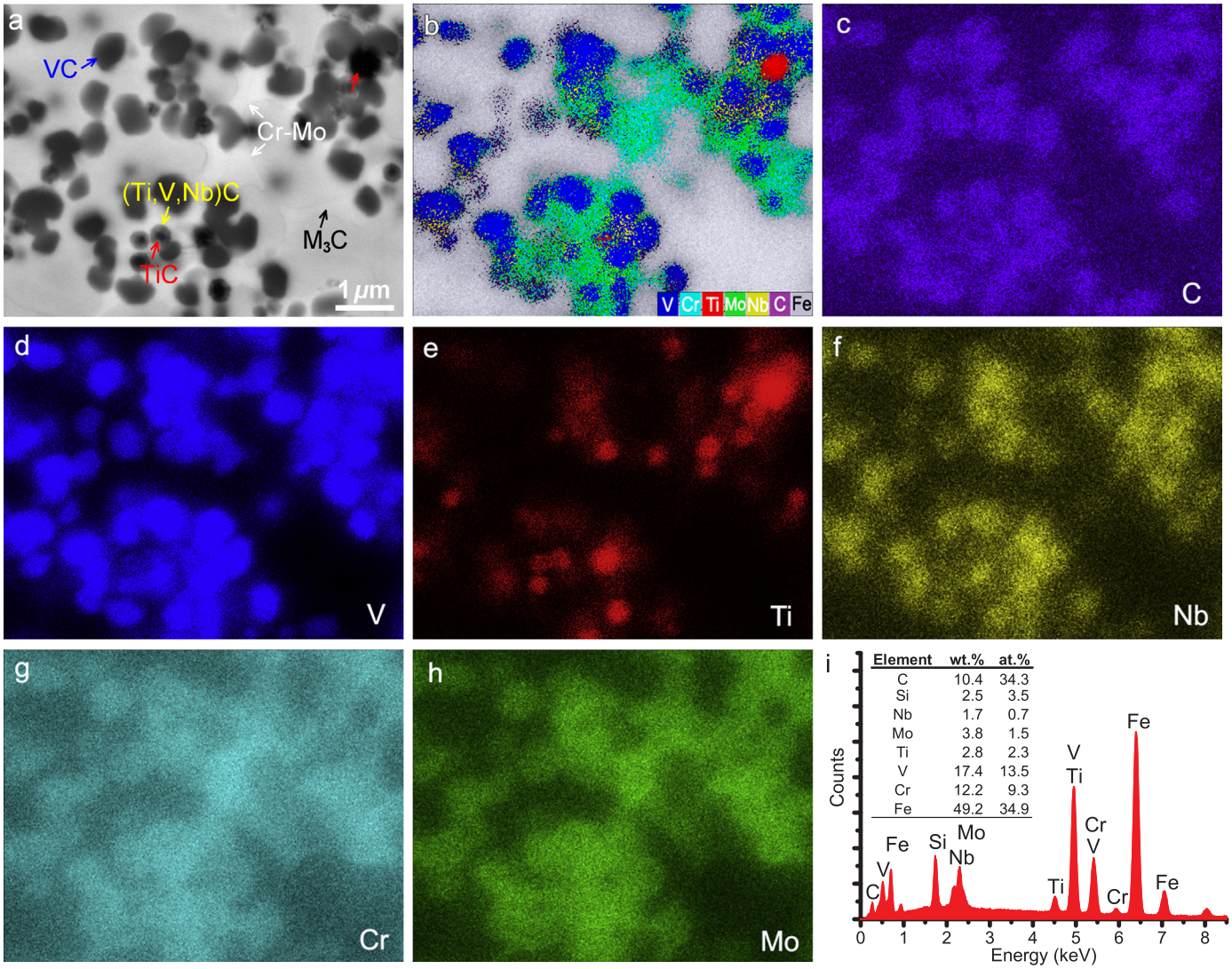

Fig. 3. EDS area mapping of the AZ: (a) SEM-BSE micrograph; (b) overlaid elements mapping; (c–h) distribution of each element as indicated; (i) EDS spectrum of the whole area of (a) and related composition quantification.

V, Ti, and Nb tend to jointly form (V, Ti, Nb)C MC-type carbide clusters whereas Cr and Mo form M_7C_3 or M_2C carbides but also dissolve into the ferrous matrix to induce solid solution strengthening [40]. VC, TiC and NbC carbides share a NaCl-type face-centered cubic (FCC) structure with small crystal lattice mismatches (a_{VC} = 0.417 nm, a_{TiC} = 0.432 nm, a_{NbC} = 0. 445 nm) and thus hold good mutual compatibility [8,18,36]. It was reported [8] that VC-TiC system fulfills Hume–Rothery condition where V and Ti atoms can be substituted without impairing the stability of FCC structure such that they can form a solid solution. Comparable conditions should also fit with the (V, Nb)C system. Similar duplex carbides were also reported in the white cast iron with a high-entropy microstructure characteristic of Ti, V, Mo, W and Cr [4].

Closer inspection displayed in Fig. 4a reveals that TiC can serve as the nucleation sites for the formation of VC, where the round TiC particles are centered inside VC crystals, in agreement with [42]. Fig. 4b illustrates the bright-field TEM image of one carbide cluster and Table 2 reveals the associated EDS results. It can be seen that spot 1 contains a comparably high content of Ti (22.3 at%) and V (22.1 at%). The total content of V, Ti and Nb (3.3 at%) equals well with that of C (48.6 at%). The content of V is enriched predominantly in spot 2, 4, whereas the upper bulk-like carbide (spot 3) tends Fe-rich (74.6 at% Fe vs. 20.3 at% C). The selected area diffraction patterns (SADP) confirm V_8C_7, VC, TiC, Fe_3C carbides at spot 1–3 (Fig. 4c–e) and a sole [001] VC at spot 4 (Fig. 4f). Note that MC_x carbides are usually substoichiometric, namely $x < 1$. For example, VC carbides can be in the type of VC, V_2C, V_4C_3, V_6C_5, V_8C_7 [43–45] due to carbon vacancies. Among them, V_8C_7 holds a super-lattice structure where the V atoms occupy positions slightly off the ideal FCC positions and the C atoms have an ordered arrangement on the interstitial sites, and it has a larger lattice (a_{V8C7} = 0.833 nm) as compared to that of VC [43,45,46]. Fig. 4c confirms that in the carbide cluster V_8C_7 can maintain a cube-on-cube orientation relationship with TiC, namely (022) TiC || (022) V_8C_7, [1$\bar{1}$1] TiC || [1$\bar{1}$1] V_8C_7. The crystal orientation of TiC/V_8C_7 duplex carbide schematically plotted in Fig. 5 indicates that they share parallel [1$\bar{1}$1] zone axis and (022) crystal planes. It can be concluded that TiC acts as a nucleation core around which MCs (M = V, Ti) grow. This is because of a more significant affinity of Ti to C, and the higher melting temperature of TiC (3140 °C) than VC (2830 °C) [38] renders earlier precipitation of TiC from the melt to serve as a favored heterogeneous nucleus. It may also apply to NbC, but the negligible content of Nb (also probably a larger crystal lattice mismatches of VC-NbC) limits it as a core. In addition, Fig. 4d confirms the relationship between zone axis [01$\bar{1}$] of TiC and zone axis [$\bar{1}$11] of another VC carbide presented at the lower-left corner in Fig. 4b (spot 2). Note that the partial substitution of V by Ti and/or Nb is beneficial because partial Ti substitution for V to form MC

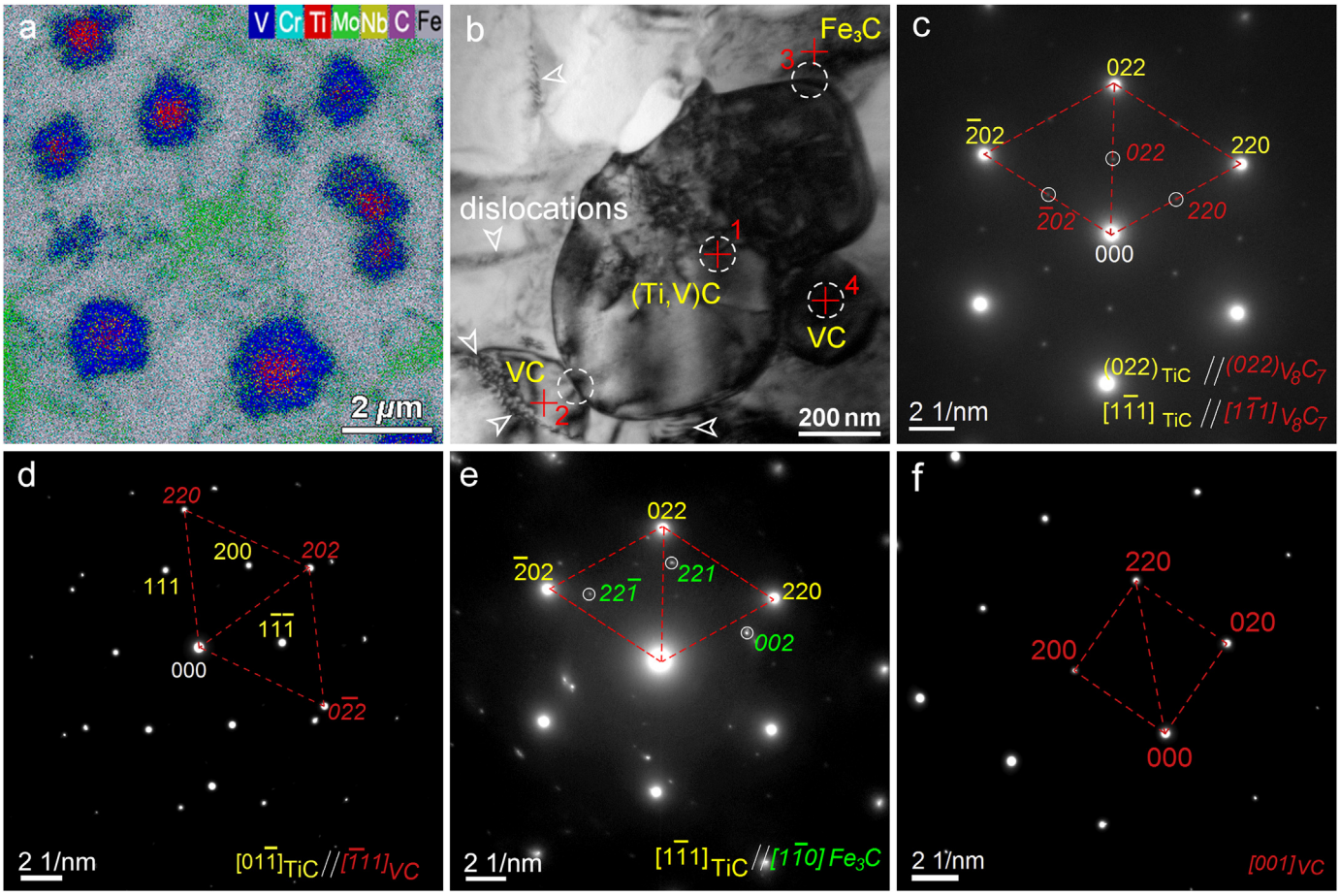

Fig. 4. (a) EDS area mapping showing TiC/V_8C_7 double carbides; (b) bright-field TEM image showing MC carbide cluster in the AZ with the crosses numbered for EDS; (c–f) related SADPs of spot 1–4 respectively indicated by circles in (b).

Table 2
EDS results of carbides in HVHSS (Bruker, 2010F TEM).

Spot	Element (at%)						
	C	V	Ti	Cr	Mo	Nb	Fe
1	48.55	22.11	22.27	0.74	0.50	3.27	2.57
2	58.03	34.32	1.01	1.43	1.87	1.67	1.67
3	20.26	1.39	1.19	1.70	0.74	0.14	74.59
4	47.83	40.28	3.08	1.32	2.25	3.32	1.91
5	48.37	41.40	1.88	1.42	2.76	2.55	1.63
6	43.35	28.54	0.04	12.23	11.53	1.25	3.05

Note: the spots for EDS are marked by the crosses in Figs. 4b and 6c.

carbides in the HSS decreases the grain size and promotes grain nucleations leading to fine-grain strengthening [37]. Both Ti and Nb can be used as a substitutional carbide-forming element to form stable MC carbides. Fig. 4e confirms M_3C carbide adjacent to the duplex TiC/V_8C_7, where M primarily refers to Fe, but also a bit of Cr, considering that the content of Fe is roughly three times that of C as shown in Table 2 (spot 3). M_3C (M = Fe, Cr) can change to M_7C_3 once the Cr content exceeds about 10 wt% [47].

Fig. 6a shows that certain clustered MC carbides are largely intertwined by the bulk-like carbides. The marked linear EDS as shown Fig. 6b confirms the higher Cr content, which can be determined as M_7C_3. Fig. 6c and d show the bright- and dark- field TEM micrograph of a beanlike carbide. EDS in Table 2 reveals that spot 5 is predominately V-rich, and a high content of Cr arises at spot 6. These two areas are further determined as VC and Cr_7C_3 respectively by SADPs as shown in

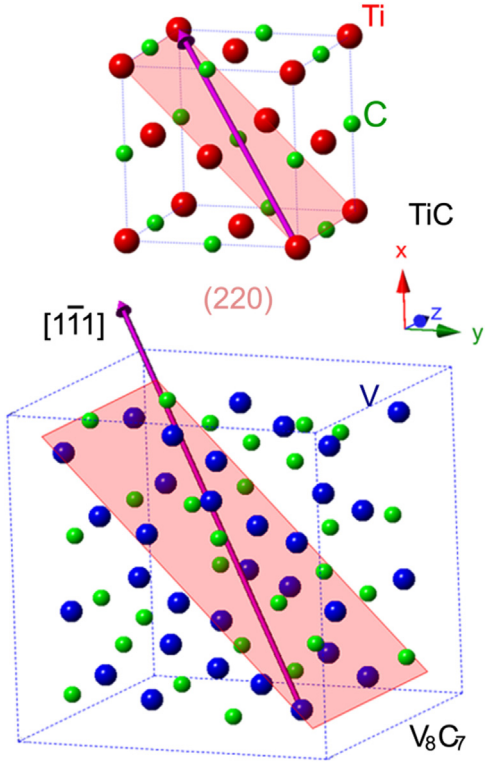

Fig. 5. Schematic model of TiC/V_8C_7 carbides elucidating the crystallographic relationship of [1 1 1] TiC || [1 1 1] V_8C_7, (220) TiC || (220)V_8C_7. Note a_{TiC} = 0.432 nm, a_{V8C7} = 0.833 nm.

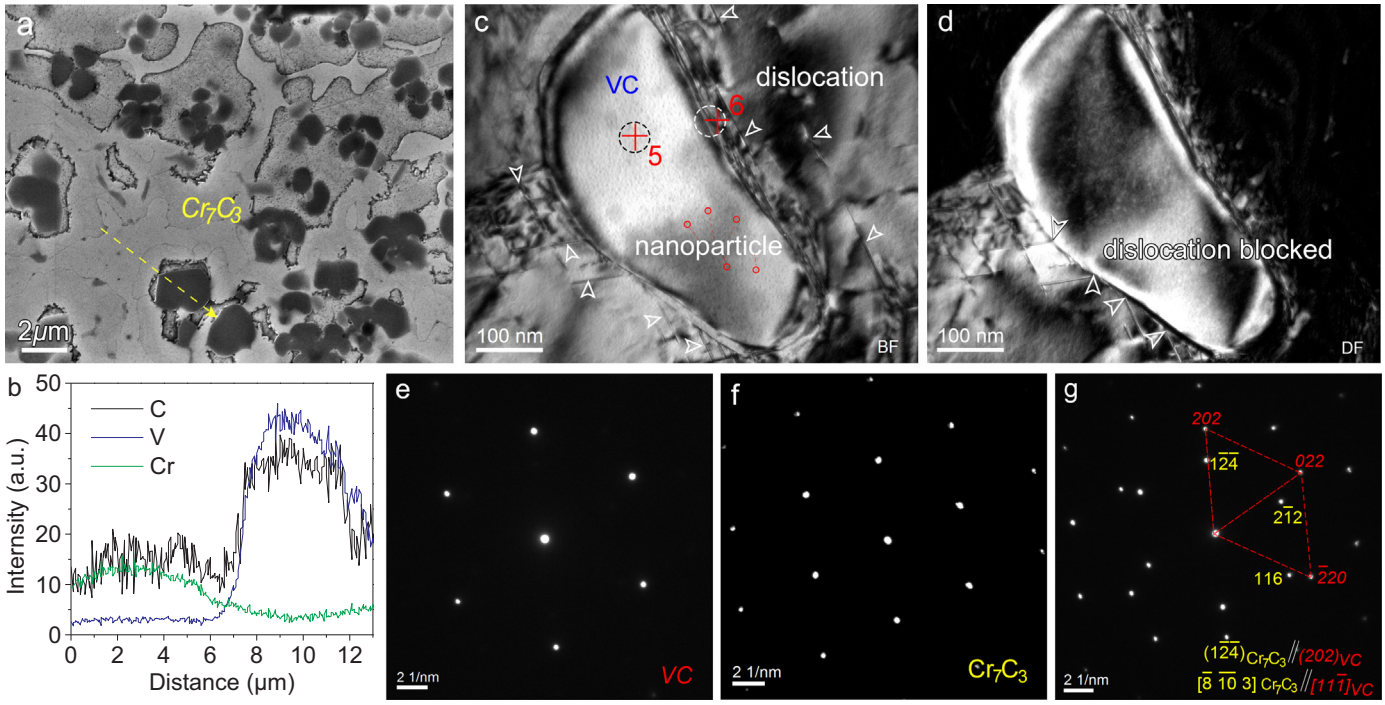

Fig. 6. (a) SEM image of M_7C_3 carbides surrounding MC carbides; (b) linear EDS along the line marked in (a) confirming high Cr content in the bulk-like carbides; (c–d) bright field and dark field TEM images of a bean-like carbide particle. Open arrows indicate stacking dislocations pass through M_7C_3 or M_3C carbides but stop moving on confronting a stronger MC. Dislocation loops induced by nanoparticles are formed in the bean-like VC; (e–f) related SADPs of spot 5 and 6 in (c) respectively; (g) SADP confirming the orientation relation of Cr_7C_3 and VC.

Fig. 6e and f. In particular, Fig. 6g confirms the crystal relationship of $(202)_{VC}$ || $(1\bar{2}4)_{Cr7C3}$, $[11\bar{1}]_{VC}$ || $[8\bar{1}\bar{0}3]_{Cr7C3}$.

Fig. 7 shows that, due to the complex non-equilibrium reactions during the plasma melting process, the high-carbon martensite (α') can form in the AZ, which may further strengthen the coating. The enlarged inset in Fig. 7a shows numerous twined martensite coexist with TiC, VC, Fe-rich M_3C and the retained austenite. TEM image (Fig. 7b) confirms the lenticular martensite. The associated SADP (Fig. 7c) determines it as a typical {112} < 111 > twined martensite with [011] zone axis. The retained austenite that surrounds the martensite is also confirmed (Fig. 7d). The alloying elements such as V, Ti, Nb, Cr, Mo all decrease the martensite transformation starting temperature (Ms) which promotes martensite transformation whereas the rapid cooling rate in the PSA process renders the incomplete transformation of martensite into austenite and thus some austenite remains.

3.2. Phases

Fig. 8 shows the XRD spectra of the NCI substrate and high-V alloyed coating. For the untreated NCI substrate, only the diffraction peaks of ferrite (α) and graphite can be indexed. For the coating, carbide phases besides α were formed and can be identified as MC and M_2C (M = V, Ti, Nb and Mo) type carbides together with Cr-rich M_7C_3 and $M_{23}C_6$ carbides. The high cooling rate in the PSA process increases the solubility of alloy elements in the matrix [5], thereby rendering alloy elements into the matrix to form ternary precipitates [50] such as $Mo_2V_4C_5$ [JCPDS No.: 65-8769] and $Ti_{0.42}V_{1.58}C$ [JCPDS No.: 65-7965]. Note that Fe-rich M_3C, martensite and retained austenite were also detected, in accordance with SEM and TEM observations (see Fig. 3a and Fig. 7). The added alloying elements stabilize austenite and the PSA process offers insufficient time to complete the austenite-martensite transformation leading to retained austenite. We can thus conclude that the AZ may be strengthened by hierarchical hard phases including alloy carbides, twined martensite and cementite that are all together embedded in a ductile ferrite and retained austenite matrix.

During the PSA process, primary MC-type carbides first solidify due to their highest melting temperature and stabilize in the melt. V, Ti, Nb are strong carbide-forming elements that first bond to C to form carbides. Correspondingly, Cr-carbides are later formed because of its relatively low melting point (1520–1780 °C) [41]. L→ (γ-Fe + MC) eutectic reaction occurs when the melt arrives at the eutectic composition and temperature. Continuous formation of eutectic MC leads to the depletion of M (M = Ti, Nb, V) elements and increase in the relative content of Cr and Mo in the remaining liquid, and eventually leads to L→(γ-Fe + M_7C_3 + $M_{23}C_6$ + M_2C) eutectic reactions. With decreasing C content, the carbide-forming elements Cr and Mo tend to become superfluous and start to play a role for the saturation of the ferrous matrix as confirmed in Fig. 3g and h.

3.3. Mechanical properties

3.3.1. Crack resistance and hardness

Nanoindentation was executed to compare the microhardness of three zones as well as the crack resistance. The maximum indentation depth was set to 800 nm for all the zones. This indent has a transverse length above 5 times of the size of carbides (1 μm). The distance between two adjacent impressions is 30 μm avoiding possible mutual cross-talk of indentation-induced deformations (see Fig. 9a). Fig. 9b illustrates an enlarged view of one indent and it is found that after the three-sided Berkovich indentation, the coating shows characteristic smooth shear bands inside the cavity, which is supported by the AFM topographical contrast along depth profile of the indenter (see Fig. 9c). Minor micro-cracks are induced at the grain boundaries of carbide clusters located at the edges of imprints where materials are most severely deformed (indicated by the stroked black arrows in Fig. 9b). Moreover, the AFM image shows a distinct plastic pile-up with a height of ~ 100 nm above the indent, which points to a plastic deformation triggered in the coating. The AFM image also indicate some shear bands on the edge of the indentation cavity. Fig. 9d presents the nanoindentation loading and unloading curves in three zones. The

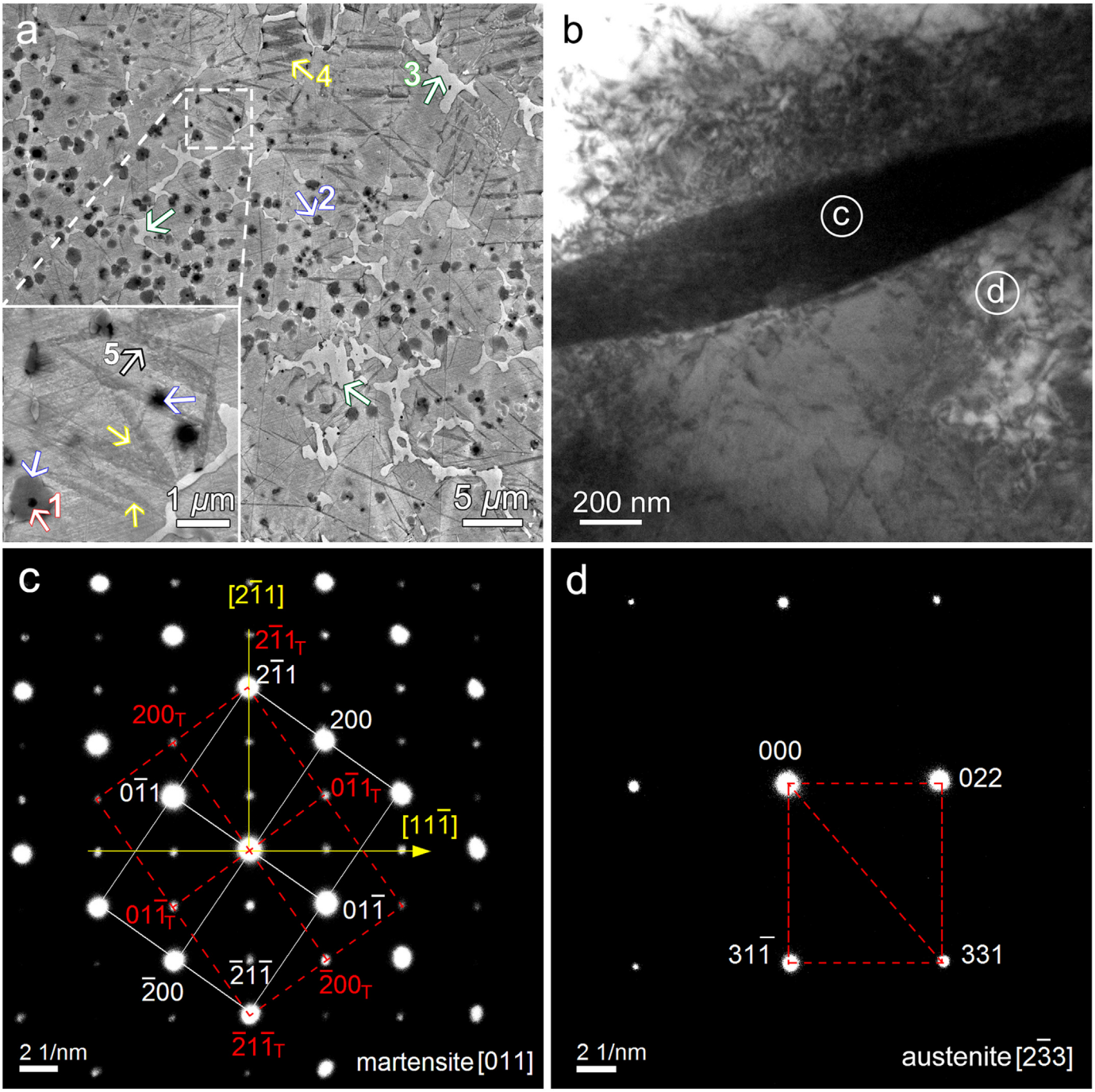

Fig. 7. (a) SEM image of martensite and austenite in the AZ (particularly adjacent to the AZ/MZ interface) together with diverse carbides (1-TiC, 2-VC, 3-Fe_3C, 4-twined martensite and 5-retained austenite as indicated respectively); (b) TEM image of lenticular twined martensite; (c, d) SADPs of the martensite and retained austenite marked in (b) respectively.

averaged hardness of the AZ is up to ~ 9.6 ± 1.0 GPa, four times as high as that of the NCI substrate (2.4 ± 0.9 GPa), although slightly lower than that of the MZ (~ 10.0 ± 1.8 GPa).

A Vickers tip was further employed to induce more severe deformations under a higher load of 50 N (beyond 400 times as that of nanoindentation). As can be seen, Fig. 10a reconfirms a smooth and continuous surface of the AZ indent cavity, and a close-view at the corner (Fig. 10b) still presents no obvious cracks. Only a few coarse primary MC carbides situated at the edges are cracked but soon blunted by the matrix. In contrast, Fig. 10c and d indicate that prevalent intergranular cracks (along with the grain edges of martensite or cementite) and transgranular cracks (passing through the cementite) are propagated both in the cavity and near the vicinity of the indentation of MZ. For instance, Fig. 10d reveals a crack penetrating through the center of a cementite plate in the lower-left corner of the indentation. In the case of the NCI substrate, the superior plasticity of ferrite results in a smoothly indented surface as shown in Fig. 10e. However, Fig. 10e and f indicate that intergranular cracks may form along the ferrite grain-boundaries or propagate through the soft graphite nodules. Above-mentioned analysis indicates that HVHSS coating promotes a high hardness combined with toughness.

3.3.2. *Residual stress and fractography*

For clad coatings by surface melting techniques, residual stresses are

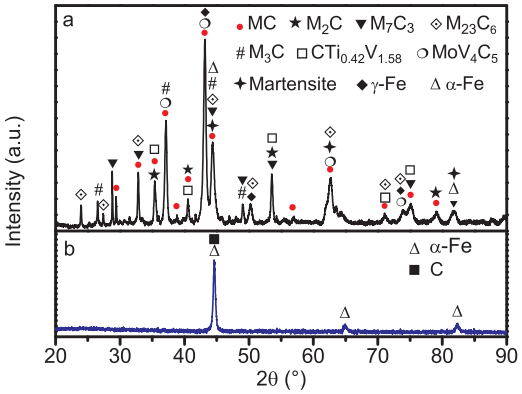

Fig. 8. XRD spectra of the plasma alloyed coating (a) and NCI substrate (b).

always a concern for engineering applications. The residual stresses in different zones of the coatings were measured by micron-sized slitting and imaging correlation method. Five micrometer-sized slits were made each at both AZ and MZ parallel along the thickness direction of the coating. Fig. 11a and b show two DIC maps of relative displacement perpendicular to the slit after to the release of the residual stresses due to FIB slitting in the AZ and MZ, respectively. As illustrated, displacements of decorating particles are similarly towards the milled slits, revealing the compressive residual stresses in both the AZ and the MZ. The residual stress was estimated as -225 ± 72 MPa and -107 ± 35 MPa in the AZ and MZ, respectively. Note that the averaging method presented by Mansilla et al. [36] was employed to calculate the fitted σ such that the displacements along the lines parallel to the slits were averaged prior to fit to Eq. (1). It is thus concluded that both the AZ and MZ have a compressive residual stress that gradually reduces towards the substrate. This is likely attributed to the large thermal gradient across the entire coating and tightly-distributed manifold carbides formed in the AZ that have a substantial difference in the coefficient of thermal expansion against the matrix. Note that a moderate level of compressive stress is beneficial for suppressing tensile crack propagation and contact fatigue of coatings.

The fractography of the AZ, the MZ and the substrate are shown in Fig. 12. Fig. 12a and b indicate that, apart from minor quasi-cleavage features, a large number of dimples and microvoids (indicated by the red arrow in Fig. 12b) predominately occur over the whole fractured surface of the AZ. The M-C (M = V, Ti, Nb) carbides are of strong covalent bonds and do not deform at the same rate as the matrix. This causes localized stress at the interface and consequently microvoids are nucleated to accommodate the incompatibility. Due to the high density of submicron-sized MC carbides, the induced voids grow sufficiently to link up until ultimately fracture with distinct dimple-dominated fractured appearance, which generally suggests substantial underlying plastic deformations pointing at a superior toughness of the AZ considering its high hardness as measured.

In contrast, Fig. 12c and d confirm that in the MZ quasi-cleavage facets dominate with the so-called river patterns resembling the distribution patterns of lathy cementite and tearing ridges are also observed, in agreement with that in the white cast iron [48]. Micro-cleavage occurs due to a high stress with a high rate of deformation. The micro-cleavage originates from the intercrystalline cracks (yellow arrows) along grain boundaries and partial transgranular fracture passing through the cementite of a relatively low hardness as confirmed in Fig. 10d. They predominately initiate from the tip or sharp corners of the blocky cementite and lenticular martensite which possess high-stress concentrations. Less shallow dimples are embedded within the cleavage facets, probably due to the contribution of the relatively ductile retained austenite in the MZ [49]. The fractured facets and minor plastic deformations demonstrate a heavy loss in toughness and an increase of brittleness in MZ.

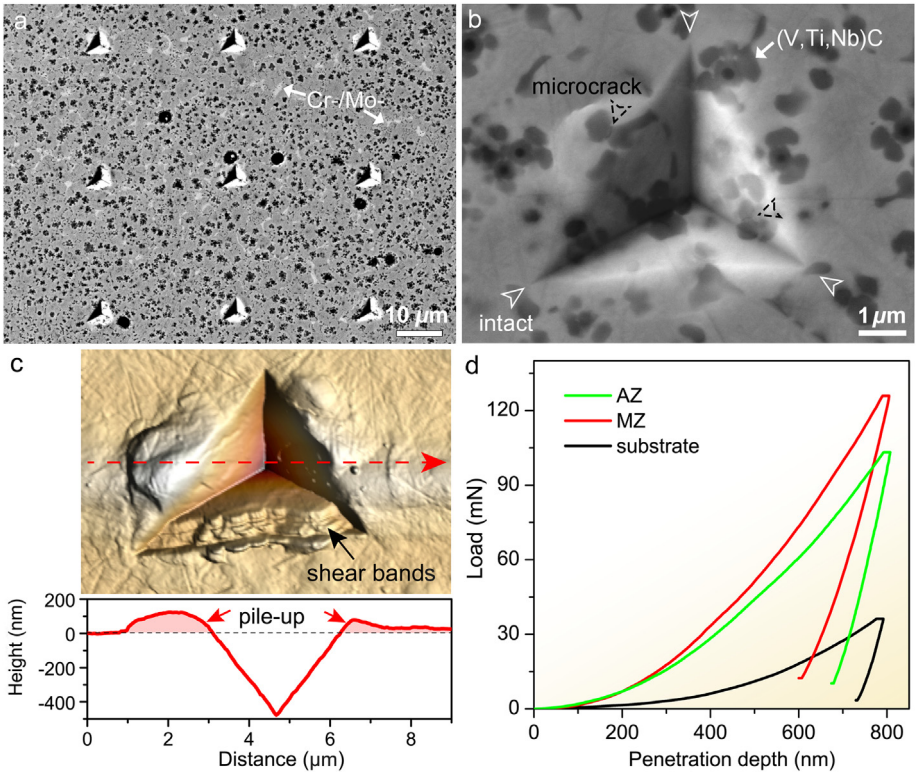

Fig. 9. (a, b) Nanoindentations on the AZ; (c) AFM image of a indent showing plastic deformation (pile-up) on the face and shear bands in the cavity; (d) typical load-depth curves of nanoindentation in three zones of the coating, together with an AFM image of a indent showing a plastic deformation (pile-up). Note that the indicated whitish particles in (a) are Cr-/Mo-carbides and the black particulate clusters in (b) are (V, Ti, Nb)C carbides.

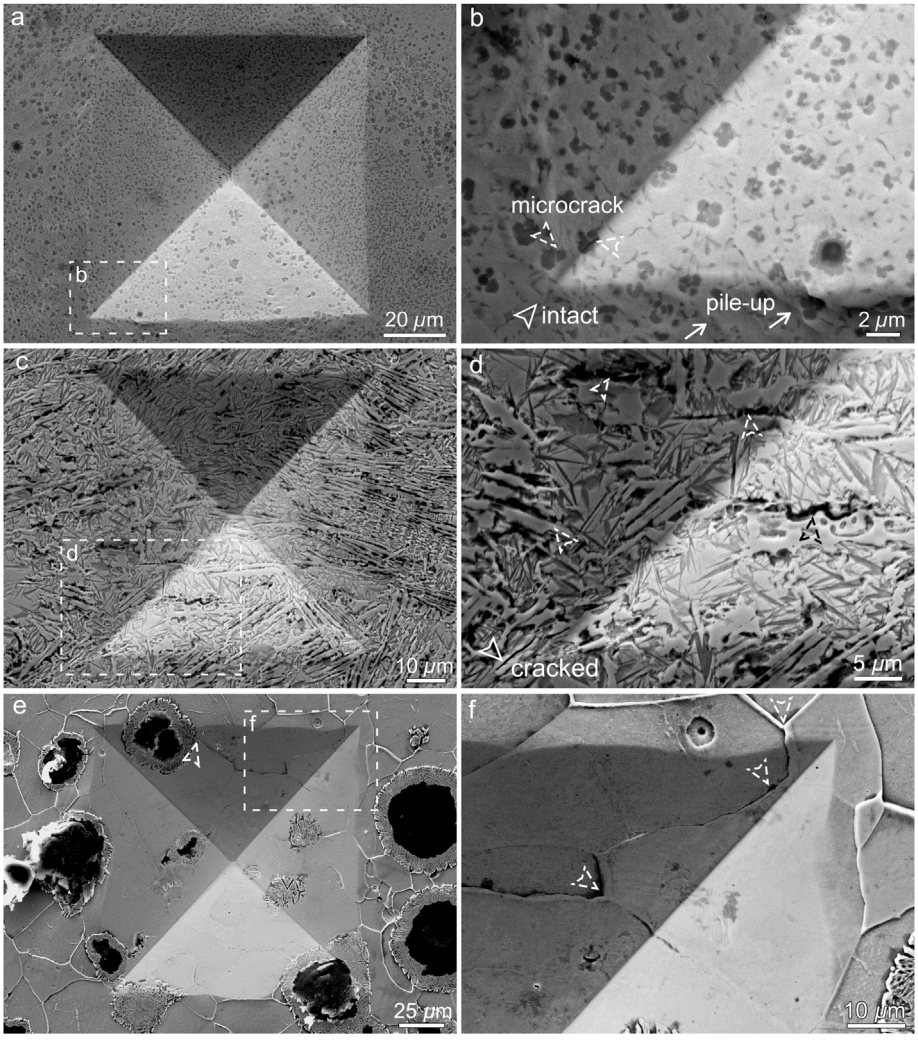

Fig. 10. Vickers impression under a high load of 50 N made in: (a–b) the AZ; (c–d) the MZ; (e–f) the NCI substrate. (b), (d) and (f) are enlarged views of the impression corners marked in (a), (c) and (e), respectively. Microcracks are indicated with the stroke arrows.

Fig. 12e and f show that a number of large cleavage facets intermingled with pockets of microcracks are characteristic of brittle fracture mechanism occurring in both the HAZ and substrate. In particular, the HAZ (see the top part of Fig. 12e) has dominated with small sharp cleavage facets due to the large prevalence of high-carbon martensite which induces high localized stress state. Many transgranular cracks are initiated and it correlates with a substantial reduction in toughness. Fig. 12f shows that cracks obviously initiate from the graphite nodules, and then propagate along the ferrite grain boundaries. Nodules normally act as potential sources of crack nucleation in irons [50].

4. Discussions

Based on the abovementioned analysis, we can see that the three distinct zones of the graded coating exhibit a rather different mechanical behavior. In particular, the AZ and the MZ exhibit comparable hardness but perform differently in stress cracking resistance and fracture. In general, refractory ceramic carbides (e.g. MC) provide much higher hardness than cementite and martensite and hence greater resistance to failure. However, note that the resistance to cracks propagation and even wear of carbide reinforced coating is determined not only by the hardness of carbides, but also by their size, volume, distribution and shape.

The sizes of the MC particles were in the range of 0.5–2 μm (with a spacing distance between particles within < 5 μm as seen in Fig. 2c) and their volume fraction could reach above 31%. In comparison to the typical size of as-cast HVHSS [22], the MC particles formed in the AZ are at least one order of magnitude smaller. According to the Hall-Petch law ($\sigma = \sigma_0 + Kd^{-1/2}$, where σ is the yield stress, σ_0 is the friction stress, K reflects the obstacle strength of grain-boundaries (Hall-Petch slope), and d is the average grain diameter [51]), it can be expected that the efficient grain refinement induced by the joint effects of the rapid cooling rate in PSA and heterogeneous nucleation can significantly enhance the strength of the alloyed coating. Still, the uniform distribution of primary MC reinforcements formed in the coating serves as grain growth inhibitor for prior austenite via Zener pinning effects [52], leading to refined and homogeneous phase transformation products after solidification [53]. Fig. 6c and d indicate that MC carbides retard the dislocation movement and thereafter make their subsequent motion more difficultly.

Plenty of stacking faults marked by the arrows even stop moving on confronting the stiff MC carbides. Additional force is thus needed for those dislocations to overcome the barriers. In particular, Fig. 13a confirms a multiplication of dislocation (pile-up) occurring around and or between the tightly-distributed carbide clusters. It also indicates that the spacing between the MC carbides can be < 200 nm, which meets the criterion for the Orowan strengthening mechanism usually operating at an inter-particle distance < 500 nm depending on the size [54]. Furthermore, apart from the submicron-sized (primary) MC, in the HVHSS coating there are still numerous ever smaller nano-sized

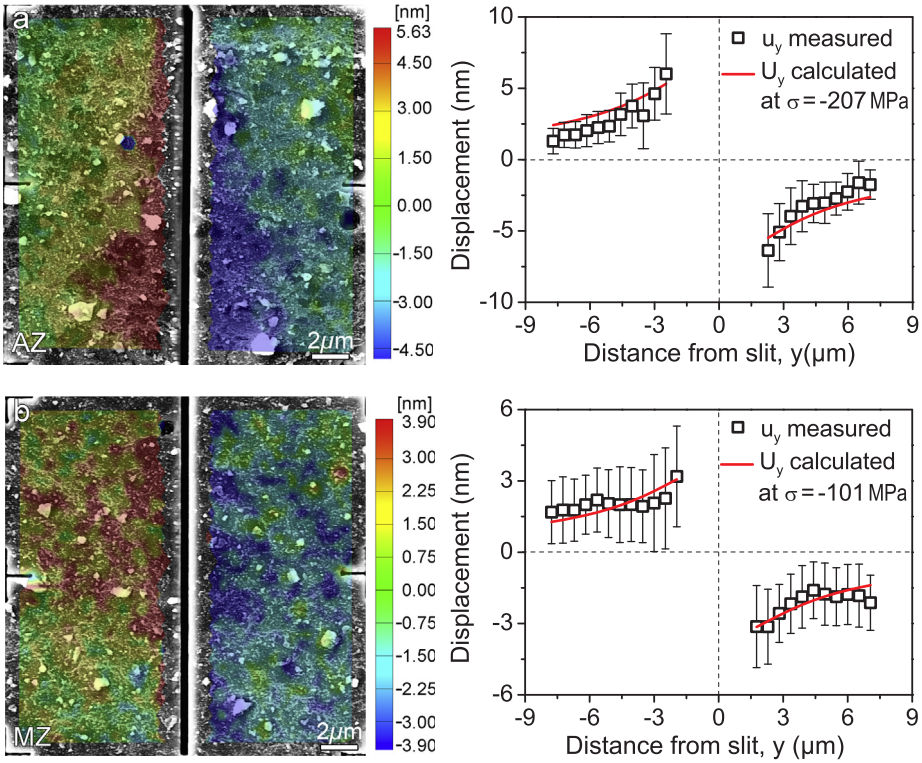

Fig. 11. Typical FIB-slit overlaid with surface displacement field after stress release from DIC analysis and plot of the measured displacement against the calculated displacement based on the matched compressive residual stress: (a) the top AZ and (b) the middle MZ.

(eutectic) MC carbides [40,55] that potentially pin the dislocations leading to reinforcement.

Xu et al. [22] compared the wear behaviors of as-cast HVHSS and high-chromium white iron under rolling contact and found that dislocation cells are formed within VC carbides due to the pining effects of ultrafine nanoparticles composed of (V, Mo, Fe, Cr)C [22]. Similar nanoparticles are observed in Fig. 6c. It can therefore be concluded that VC consists of a hierarchical structure where its interior nanoparticles are supposed to absorb impact energy and thus resist crack initiation inside the VC, making the pisiform VC remain intact. In contrast, localized slip bands in M_7C_3 (also possible M_3C) are observed. Once the slip is blocked, stress concentration arises and this may lead to easy crack initiations inside M_7C_3. This proves MC carbides have improved trans-granular and inter-granular slip resistance in comparison to M_7C_3 type.

It should be pointed out that Fig. 9c indicates that the AZ has a hardness only around 10 GPa. This is understandable because the measurement is representing an 'apparent' hardness taking into account the combined effects of the soft matrix apart from the hard reinforcing carbides. More surprisingly is that both the nano- and micro-indentation do not lead to apparent cracks at the corners (Fig. 9 and 10), which points to a superior ductility in AZ. The plastic flow near the vicinity of the indent (see Fig. 9c) confirms an enhanced fracture strength and toughness.

The accumulation of dislocation pile-up comes from the successive out-of-plane displacement events encouraged by rotation and reorientation of the crystals in a favored crystallographic glide direction under the indenter tip [56]. In fact, Minor et al. [57] and Soer et al. [58] reported that the onset of plasticity commences under indenter contact provided with dislocation rearrangement of preexisting dislocation and subsequent propagation. The high collective mobile dislocation density accommodates a large plasticity upon yielding [59]. Fig. 4b and Fig. 13b confirm a network of mobile dislocations evidently visible around the MC carbides, where the grain boundary migration and dislocation sliding help mediate the heterogeneous plastic deformation [59,60]. In addition, the weaker ferrite-austenite matrix also provides easy pathways for the dislocation motion, as verified by the densely interconnected dislocation indicated in Fig. 13c and d of the coating matrix area. It is known that the dual-phase matrix composed of austenite and ferrite allows a significant persistent elongation [61].

Several indentations and fractography shown in Figs. 9, 10 and 11 indicate a superior fracture crack resistance of the AZ despite that originally hard but brittle ceramic carbides are substantially incorporated into the coating. This can be ascribed to the following reasons:

(a) Grain refinement. Due to the ultrafine carbides embedded in a ductile matrix leading to an increase in mechanical strength not necessarily accompanied by huge ductility reduction (size effects). Karch et al. [60] reported that conventionally brittle ceramics could become ductile, permitting plastic deformations due to diffusional creep along abundant intercrystalline interfaces by decreasing size of ceramic particles;
(b) Dispersion strengthening. The uniform dispersive structure with no cellular or blocky dendrites and the high volume fraction of spherical or near-spheroidal shaped carbides help to evenly distribute the stress/strain. Although the overall residual compressive stress is higher in the AZ as compared to MZ, the ductile matrix surrounding around carbides allow the transfer and distribution of the applied load from the reinforcement phases to the ductile matrix [1];
(c) Crack deflection. As illustrated in Fig. 14a, multiple hard ceramic particles obviously appear to drive the cracks to grow along the perimeter of carbides (largely deflected) [62] near the edge of a Vickers indentation. The relatively high compressive stress field (see Fig. 11) normal to the crack can help restrain crack tip opening and thus increase the force needed for crack propagation. The schematics of crack propagation in the AZ, MZ and substrate are displayed in Fig. 14b–d, respectively. The more tortuous crack path (corresponding to a prolonged propagating distance) in the AZ is a direct sign that more energy must be consumed during crack

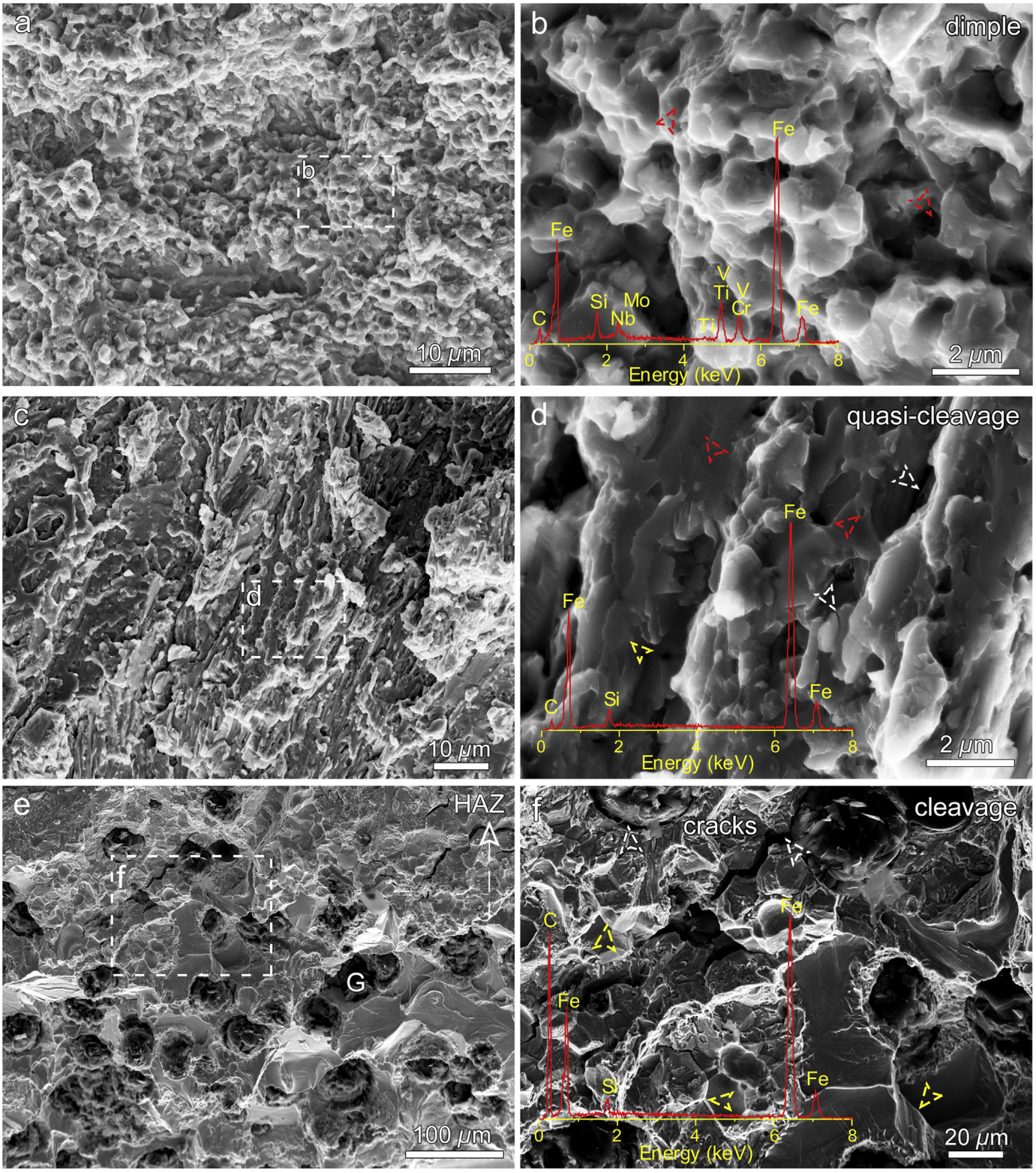

Fig. 12. Room-temperature fracture morphologies of (a, b) the AZ, (c, d) the MZ and (e, f) the HAZ and NCI substrate. Note that (b), (d) and (f) are close-views of the marked areas in (a), (c) and (e), overlaid with the corresponding EDS spectra. Stroked arrows colored in red, yellow and white refer to microvoids, cleavage facets and microcracks respectively.

spreading [19]. The crack deflection also reduces the stress intensity at the crack tip [63]. In addition, the inset in Fig. 14a indicates that MC particles on the way of propagating cracks could bridge them. Crack bridging and pullout lead to efficient energy dissipation and substantial increase in the fracture toughness [64].

In contrast, cracks may propagate along the lathy cementite (M_3C) and also the edge of twined martensite (α') in the MZ (Fig. 10d and Fig. 14c). In such case, the cracks continue advancing straightly once initiated because of minor blocking defections. The sharp irregular shape of martensite and cementite also readily triggers tip

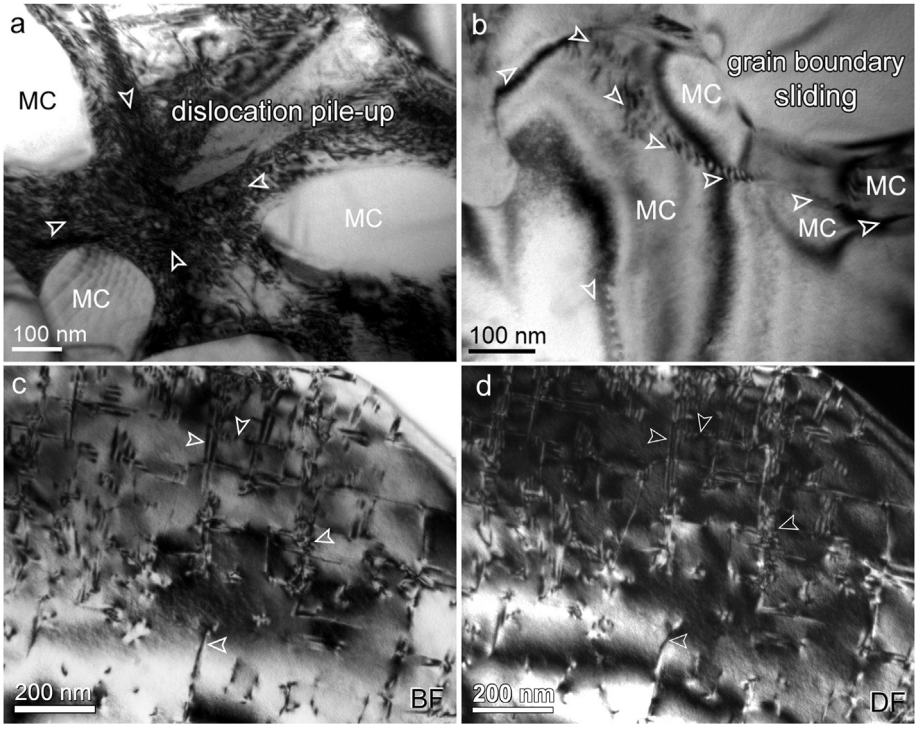

Fig. 13. Hard and toughening mechanism: (a) dislocation (indicated by arrows) pile-up between the strong MC carbide clusters; (b) grain boundary dislocation sliding along the grain boundaries of MC carbide; (c–d) BF- and DF-TEM images of the alloying matrix rich with interconnected dislocations network explaining for plasticity.

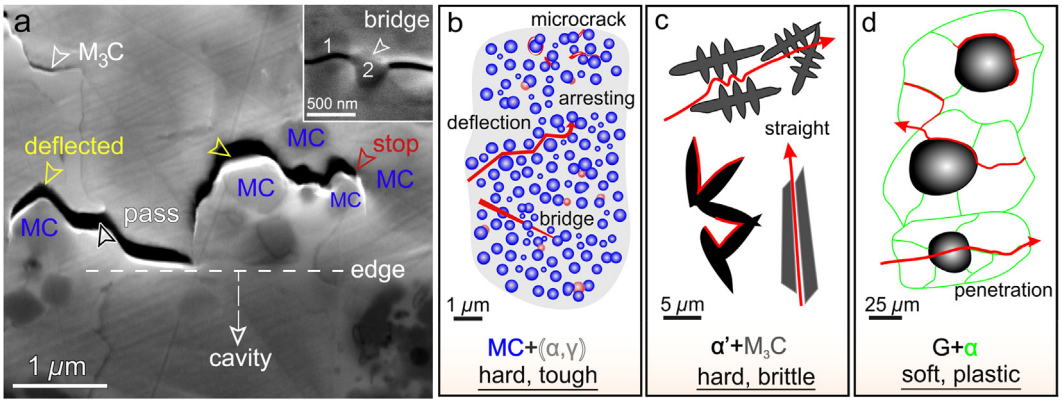

Fig. 14. (a) Microcracks are deflected by the spherical MC carbides near the edge of an indentation in AZ, with the inset showing the bridging effect of MC carbides on the way of crack propagation; (b–d) schematics of potential crack growing routes in the AZ (b), MZ (c) and NCI substrate (d) respectively.

uneven localized stress concentration. Both explain the presence of large cracks as observed in Fig. 10d. Furthermore, while the hard MC carbides could hamper the crack front propagation (Fig. 6d and Fig. 10b), the crack instead readily penetrates the dendritic arms of the cementite endowed with a low hardness (see Fig. 10d and Fig. 14a). In the case of NCI substrate, due to the low hardness of ferrite and graphite nodules and particularly the absence of strong obstacles, cracks can easily nucleate and pass, preferably along the grain boundaries starting from the graphite nodules (Fig. 12f and Fig. 14d).

(d) Crystal structure of the constituents. It is well-known [65] that BCC metals (e.g. martensite in MZ and ferrite in the NCI substrate) tend towards cleavage fractures towards (001) crystal planes along [111] glide direction while the FCC structure (e.g. the γ-Fe and all MC in the AZ) seldom yield cleavage fracture thanks to its multiple sliding bands and low dislocation emission stress [66]. This is compatible with the comparisons of SEM observations in Fig. 12b, d and f. Analysis of Fig. 10f and the obvious cleavages in Fig. 12f demonstrate that the ferrite-dominated so-called ductile iron substrate is rather plastic but not actually tough and crack-resistant. In conclusion, the HVHSS coating (AZ) is hard-yet-tough, also with reliable plasticity and thus outperforms both the MZ and the NCI substrate considerably.

It is worth mentioning that although the MZ is hard but brittle, due to the rapid cooling rate in the PSA process, the grain size of the cementite plates is still much smaller (< 10 μm) than that of the as-cast white iron produced in a traditional induction melting furnace [67]. Moreover, the original undesirable netlike shapes [41] are fragmented into short and discontinuous bulky pieces that ultimately leads to a stress reduction (see Fig. 2d). The MZ at the subsurface can serve as a hard cushion layer supporting the top AZ coating to bear higher loads and meanwhile increases the adhesion with the substrate to protect from a catastrophic failure such as crash fragmentation. It assists such

graded HVHSS coating to become thicker and stronger potentially for harsh industrial applications.

5. Conclusions

(1) A novel MC-reinforced alloy layer-modified white iron-nodular iron graded HSS coating was directly fabricated in situ by an easy plasma surface alloying process. The top alloyed zone features with hierarchical hard phases such as MC, M_2C, M_7C_3, martensite and cementite. The refined and spherical carbides are uniformly distributed in a weak (α, γ)-Fe ductile matrix.
(2) The hardness of the coating increases up to around 9.6 GPa, with no clear impact for toughness reduction that readily occurs in brittle materials. Such an exceptional combination of strength and ductility arise from the heterogeneous nucleation and the rapid solidification rate which collectively activate a synergy of intrinsic strengthening mechanisms including hierarchically heterogeneous microstructures, grain refinement, solid solution strengthening, dislocation strengthening and grain boundary sliding.
(3) The fractured surface in the AZ shows ductile dimpled fracture whereas that in the MZ and substrate tends cleavage fracture. Microcracks propagation in the AZ are deflected /guided into the matrix and stiff MC carbides delay fracture by shielding the crack tip in a compressive residual stress field. This coating presents a new route for a superior strength-ductility-toughness combination, as compared to both the MZ consisting of martensite-reinforced ledeburite and the nodular iron substrate.

Acknowledgments

The PSA samples were prepared at the Huazhong University of Science and Technology, China and materials characterizations were conducted at the University of Groningen, the Netherlands. H.T. Cao acknowledges China Scholarship Council, P. R. China for his Ph.D. Scholarship (CSC, No. 201406160102).

References

[1] R.L. Deuis, J.M. Yellup, C. Subramanian, Compos. Sci. Technol. 58 (1998) 299–309.
[2] S.F. Zhou, X.Y. Zeng, Q.W. Hu, Y.J. Huang, Appl. Surf. Sci. 255 (2008) 1646–1653.
[3] Y.L. Yuan, Z.G. Li, Surf. Coat. Technol. 248 (2014) 9–22.
[4] Y.P. Wang, D.Y. Li, L. Parent, H. Tian, Wear 271 (2011) 1623–1628.
[5] X. Lim, Nature 533 (2016) 306–307.
[6] Z.M. Li, K.G. Pradeep, Y. Deng, D. Raabe, C.C. Tasan, Nature 534 (2016) 227–230.
[7] J.W. Yeh, S.K. Chen, S.J. Lin, J.Y. Gan, T.S. Chin, T.T. Shun, C.H. T, S.Y. Chang, Adv. Eng. Mater. 6 (2004) 299–303.
[8] Y. Zhang, T.T. Zuo, Z. Tang, M.C. Gao, K.A. Dahmen, P.K. Liaw, Z.P. Lu, Prog. Mater. Sci. 61 (2014) 1–93.
[9] T. Bhattacharjee, I.S. Wani, S. Sheikh, I.T. Clark, T. Okawa, S. Guo, P.P. Bhattacharjee, N. Tsuji, Sci. Rep. 8 (2018) 3276.
[10] S. Sheikh, S. Shafeie, Q. Hu, J. Ahlström, C. Persson, J. Veselý, J. Zýka, U. Klement, J. Appl. Phys. 120 (2016) 164902.
[11] E. Munch, M.E. Launey, D.H. Alsem, E. Saiz, A.P. Tomsia, R.O. Ritchie, Science 322 (2008) 1516–1520.
[12] P.Y. Chen, J. McKittrick, M.A. Meyers, Prog. Mater. Sci. 57 (2012) 1492–1704.
[13] J. Yi, W.H. Wang, J.J. Lewandowski, Adv. Eng. Mater. (2014) 620–625.
[14] H.D. Espinosa, J.E. Rim, F. Barthelat, M.J. Buehler, Prog. Mater. Sci. 54 (2009) 1059–1100.
[15] C.A. Wang, Y. Huang, Q.F. Zan, H. Guo, S.Y. Cai, Mater. Sci. Eng. C 11 (2000) 9–12.
[16] M. Mirkhalaf, A.K. Dastjerdi, F. Barthelat, Nat. Commun. 5 (2014) 1–9.
[17] W.J. Clegg, K. Kendall, N.M. Alford, T.W. Button, J.D. Birchall, Nature 347 (1990) 455–457.
[18] W.F. Wang, J. Mater. Eng. Perform. 11 (2002) 516–518.
[19] Y. Gu, J.X. Liu, F. Xu, G.J. Zhang, J. Eur. Ceram. Soc. 37 (2017) 539–547.
[20] J. Balko, T. Csanádi, R. Sedlák, M. Vojtko, A. Kovalčíková, K. Koval, et al., J. Eur. Ceram. Soc. 37 (2017) 4371–4377.
[21] C.C. Zhao, Y.F. Zhou, X.L. Xing, S. Liu, X.J. Ren, Q.X. Yang, Appl. Surf. Sci. 439 (2018) 468–474.
[22] L.J. Xu, J.D. Xing, S.Z. Wi, Y.Z. Zhang, L. Rui, Mater. Sci. Eng. A 434 (2006) 63–70.
[23] J.R. Davis, Alloying: Understand the Basic, ASM International, 2001.
[24] L. Bourithis, G.D. Papadimitriou, Mater. Sci. Eng. A 361 (2003) 165–172.
[25] S.H. Wang, J.Y. Chen, L. Xue, Surf. Coat. Technol. 200 (2006) 3446–3458.
[26] P. Ding, G. Shi, S. Zhou, Metall. Trans. A 24 (1993) 1265–1272.
[27] J. Ju, H.G. Fu, D.M. Fu, S.Z. Wei, P. Sang, Z.W. Wu, K.Z. Tang, Y.P. Lei, Ironmak. Steelmak. 45 (2018) 176–186.
[28] R.M.M. Riofano, L.C. Casteletti, L.C.F. Canale, G.E. Totten, Wear 265 (2008) 57–64.
[29] Y. Uematsu, K. Tokaji, T. Horie, K. Nishigaki, Mater. Sci. Eng. A 471 (2007) 15–21.
[30] A. Kasak, E.J. Dulis, Powder-metallurgy tool steels, Powder Metall. 21 (1978) 114–123.
[31] Z. Zhang, T. Yu, R. Kovacevic, Appl. Surf. Sci. 410 (2017) 225–240.
[32] F.X. Ye, M. Hojamberdiev, Y.H. Xu, L.S. Zhong, N.N. Zhao, Y.P. Li, X. Huang, Appl. Surf. Sci. 280 (2013) 297–303.
[33] J.J. Feng, C.X. Pan, L.L. Lu, Q.W. Huang, H.T. Cao, J. Iron Steel Res. Int. 23 (2016) 618–624.
[34] Y.F. Liu, J.M. Han, R.H. Li, W.J. Li, X.Y. Xu, J.H. Wang, S.Z. Yang, Appl. Surf. Sci. 252 (2006) 7539–7544.
[35] H.T. Cao, X.P. Dong, Q.W. Huang, Z. Pan, J.J. Li, Z.T. Fan, Int. J. Miner. Metall. Mater. 21 (2014) 363–370.
[36] C. Mansilla, D. Martínez-Martínez, V. Ocelík, J.T.M. De Hosson, J. Mater. Sci. 50 (2015) 3646–3655.
[37] D. Galvan, Y.T. Pei, J.T.M. De Hosson, Acta Mater. 53 (2005) 3925–3934.
[38] I. Hemmati, V. Ocelík, J.T.M. De Hosson, Mater. Sci. Eng. A 582 (2013) 305–315.
[39] M. Ulutan, K. Kiliçay, O.N. Çelik, Ü. Er, J. Mater. Process. Technol. 236 (2016) 26–34.
[40] H.T. Cao, X.P. Dong, S.Q. Chen, M. Dutka, Y.T. Pei, J. Alloy. Compd. 720 (2017) 169–181.
[41] H.T. Cao, X.P. Dong, Z. Pan, X.W. Wu, Q.W. Huang, Y.T. Pei, Mater. Des. 100 (2016) 223–234.
[42] L.A. Dobrzanski, M. Ligarski, J. Mater. Process. Technol. 9244136 (1997) 101–116.
[43] L.L. Wu, T.K. Yao, Y.C. Wang, J.W. Zhang, F.R. Xiao, B. Liao, J. Alloy. Compd. 548 (2013) 60–64.
[44] X.L. Cai, L.S. Zhong, Y.H. Xu, Z.X. Lu, J.L. Li, J.L. Zhu, Y.C. Ding, H.H. Yan, J. Alloy. Compd. 747 (2018) 8–20.
[45] V.N. Lipatnikov, A.I. Gusev, P. Ettmayer, W. Lengauer, J. Phys. Condens. Matter 11 (1999) 163–184.
[46] X.Y. Chong, Y.H. Jiang, R. Zhou, J. Feng, Sci. Rep. 6 (2016) 5–13.
[47] H.T. Angus, Cast Iron: Physical and Engineering Properties, 2nd ed., Butterworth-Heinemann, 1976, pp. 253–354.
[48] M. Çöl, F.G. Koç, H. Öktem, D. Kir, Wear 348–349 (2016) 158–165.
[49] C. García-Mateo, F.G. Caballero, Mater. Trans. 46 (2005) 1839–1846.
[50] M.B. Karamış, K. Yıldızlı, Mater. Sci. Eng. A 527 (2010) 5225–5229.
[51] R.A. Masumura, P.M. Hazzledine, C.S. Pande, Acta Mater. 46 (1998) 4527–4534.
[52] E. Nes, N. Ryum, O. Hunderi, Acta Metall. 33 (1985) 11–22.
[53] B.B. He, M.X. Huang, Metall. Mater. Trans. A 49 (2018) 1433–1438.
[54] C.S. Kaira, C. Kantzos, J.J. Williams, V. De Andrade, F. De Carlo, N. Chawla, Acta Mater. 144 (2018) 419–431.
[55] H.T. Cao, X.P. Dong, Y.T. Pei, Int. J. Comput. Methods Exp. Meas. 6 (2017) 540–550.
[56] K. Yalamanchili, R. Forsén, E. Jiménez-Piqué, M.P.J. Jöesaar, J.J. Roa, N. Ghafoor, M. Odén, Surf. Coat. Technol. 258 (2014) 1100–1107.
[57] A.M. Minor, S.A. Syed Asif, Z.W. Shan, E.A. Stach, E. Cyrankowski, T.J. Wyrobek, O.L. Warren, Nat. Mater. 5 (2006) 697–702.
[58] W.A. Soer, J.Th.M. De Hosson, A.M. Minor, Z. Shan, S.A.S. Asif, O.L. Warren, Appl. Phys. Lett. 90 (2007) 181924.
[59] B.B. He, B. Hu, H.W. Yen, G.J. Cheng, Z.K. Wang, H.W. Luo, M.X. Huang, Science 177 (2017) 1–9.
[60] J. Karch, R. Birringer, H. Gleiter, Nature 330 (1987) 556–558.
[61] S.S. Sohn, H. Song, M.C. Jo, T. Song, H.S. Kim, S. Lee, Sci. Rep. 7 (2017) 1–9.
[62] L. Perrière, R. Valle, L. Mazerolles, M. Parlier, J. Eur. Ceram. Soc. 28 (2008) 2337–2343.
[63] K. Yoshida, N. Nishiyama, Y. Shinoda, T. Akatsu, F. Wakai, J. Eur. Ceram. Soc. 37 (2017) 5113–5117.
[64] P.F. Becher, J. Am. Ceram. Soc. 74 (1991) 255–269.
[65] M. Kuna, Classification of fracture processes, Finite Elements in Fracture Mechanics: Theory - Numerics - Applications, Springer Netherlands, Dordrecht, 2013.
[66] Z.C. Luo, R.D. Liu, X. Wang, M.X. Huang, Acta Mater. 150 (2018) 59–68.
[67] M. Durand-Charre, Microstructure of Steels and Cast Irons, Springer, 2013.